THERMAL DESIGN AND ANALYSIS OF CONCEPTUAL FLIGHT MODEL FOR A LUNAR EXPLORATION ROVER

*Takuto Oikawa[1], Toshiki Tanaka[2], John Walker[1], Kentaro Uno[1], Paulo Costa[3], Nathan Britton[2], Kazuya Yoshida[1]

[1] *Tohoku University, Aoba 6-6-01, Aramaki, Aoba-ku, Sendai, Japan, E-mail:* {oikawa, john, unoken, yoshida}@astro.mech.tohoku.ac.jp

[2] *ispace inc., Azabudai 3-1-6, Iikura katamachi Annex 601, Minato-ku, Tokyo, Japan, E-mail:* {t-tanaka,nathan}@ispace-inc.com

[3] *Centro Federal de Educação Tecnológica de Minas Gerais, Av. Amazonas, 5.253, Nova Suiça, Belo Horizonte, Minas Gerais, Brazil, E-mail: 201322050201@aluno.cefetmg.br*

Abstract

Currently, Team HAKUTO is developing the Flight Model version of a lunar micro rover. This rover is designed to operate during the lunar day to complete the Google Lunar XPRIZE mission requirement. Compared to the previous rover iterations, we updated the rover's thermal and power performance by incorporating passive thermal interface designs within the restricted dimension and mass budget. As part of the qualification for space readiness, alternative Commercial Off-the-Shelf avionics are implemented to replace several Pre-Flight Model phase hardware. With the fusion of a new platform, we perform thermal simulation of the rover to justify its performance within the temperature tolerant range.

1 INTRODUCTION

In recent years, space missions led by private ventures have increased significantly. The currently ongoing Google Lunar XPRIZE (GLXP) is a competition developed as an incentive to promote low cost access to the lunar surface, using an independent source outside of government funds. As of 2016, there are 16 teams participating in the competition with HAKUTO as the sole Japanese team. HAKUTO is currently in the design phase of a Flight Model (FM) lunar micro rover, codenamed Moonraker, which we are planning to send to the Moon in the second half of 2017 (Figure 1). Moonraker has undergone many phases of rover development since 2009 [1, 2]. It is built with space ready and heritage Commercial Off-the-Shelf (COTS) hardware to minimize the development and launch cost while increasing its reliability in a space environment [3]. In an effort to improve the thermal performance, HAKUTO has developed an unique multi-node passive thermal control system in order to use this hardware in the anticipated thermal lunar environment. This research covers the thermal interface design of the HAKUTO FM rover.

In a previous study, we conducted thermal vacuum testing on a Pre-Flight Model (PFM) prototype of the lunar rover to verify the thermal performance of structural
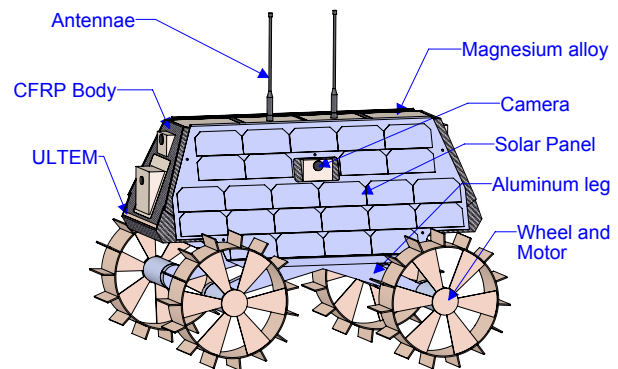

Figure 1. *: Flight model lunar rover*

materials and its interface design in preparation for FM development. Based on the experimental results, we were able to identify needed improvements, where the temperature critical components (micro-controller, battery, etc.) required extra cooling in the projected lunar mission environment [4]. Various conceptual designs for potential FM thermal interfaces, based on the PFM experimental results and lunar conditions, were conducted using trade studies [5]. A space system design approach introduced by E.W. Hammond was used as a guideline to conduct design tradeoffs in a clear and concise format to optimize the design for maximum thermal performance [6].

We present the underlying principle for the thermal design using previous satellite development's knowledge from Tohoku University on this paper [7]. As an initial step, a thermal model is developed, where the rover is broken into six different radiating surfaces. Based on the rovers orientation in reference to the solar radiative flux, its surface temperature is determined. Other thermal inputs such as lunar radiation, solar albedo, and conduction from lunar regolith are also accounted for. By using such heat conditions, a feasible mounting location for the avionics and the solar panel is determined to optimize the rovers thermal performance while retaining its compact size (∼4 kg). Once the avionics placement is fixed, the thermal isolation concept is studied to separate the radiative surfaces (avionics side) and heat absorbing surfaces

(solar panel side). This design keeps the avionics cool using reflective radiative surfaces while isolating against the heat conduction from the solar power side, which is a common technique in satellite thermal control [8]. For this paper, the final rover design configuration is discussed, and further detailed analysis is conducted using simulation software.

2 LUNAR ENVIRONMENTS AND CONDITIONS

2.1 Surface temperature model

The lunar surface temperature is modeled by Hurley et.al. [9] using the dayside Diviner data [10]. The temperature model is represented in the equation below:

$$T_l(\psi) = 392cos^n(\psi) > 130K \quad (\psi < 90°) \quad (1)$$

where ψ is defined as the solar zenith angle between the Moon-Sun line and the vector from the center of the Moon to the point on the lunar surface, n is the power factor to shape the temperature profile in the lunar day, and 130 K is the temperature at the terminator between the day and the night side. Furthermore, ψ is rearranged into a time-variant function (t) to calculate the time of day in reference to the sun's position. Parameters such as the surface temperature at a target lunar latitude (ϕ_{lat}), overall lunar inclination angle (ϕ_{inc}), and lunar synodic period (T_p) are introduced to formulate the relationship.

$$\psi(t) = \frac{2\pi}{T_p} \left| t - \frac{T_p}{4} \right| cos(\phi_{lat} + \phi_{inc}) \quad (2)$$

Hurley et. al. use $n = 0.25$ to curve fit the function close to the Diviner's lunar temperature data [9]. However, this coefficient produce some significant temperature error between the model and the Diviner data. We incorporate the proposed correction factor of $n = 0.29$ from Walker to reduce the error to within 10°C accuracy between the temperature model function and the Diviner data [11]. This temperature curve holds true at a condition of 45°latitude and between 25 hours after the sunrise and before the sunrise. The resulting temperature plot at 45°latitude is shown in Figure 2.

2.2 Mission milestone

The mission for the HAKUTO rover at the Moon is separated into two categories: the GLXP and the science mission. All of the missions are expected to be completed within a two-week timespan during the daytime. On the other hand, the lunar night side is not accounted into the mission as the rover is not expected to survive the extreme cold. Figure 2 shows the timeline of the rover's activity on the Moon, where each mission stage description is shown below:

① Expected landing time on the Moon.
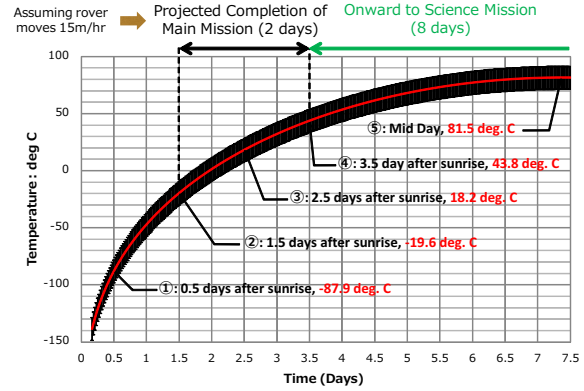
Figure 2. : *Lunar surface temperature profile at 45 degrees latitude with the mission description*

② Expected mission start time.
③ 1 day elapsed after the mission start time.
④ Expected mission end time.
⑤ The peak surface temperature on the Moon.

From the mission timeline, we are concerned mainly with two factors regarding thermal performance: 1) the appropriate start time for the competition and 2) can the rover operate through lunar mid day (81.5°). As the GLXP mission is expected to be completed in two days (assuming that the rover runs at 15 meters every hour), it is critical at a minimum to satisfy the rover's performance requirement during the two-day time period. Most of the COTS hardware implemented into the rover is capable of withstanding lunar temperatures between 1.5 days after the sunrise and mid day. However, a detailed simulation is required to verify the rover's thermal performance. As an additional mission objective, we plan to explore the sky-light near Lacus Mortis during the science mission, and survivability at mid day is critical to operate the rover for an extensive period of time [1].

2.3 Surface properties

Lunar surface thermal modeling requires three basic parameters: albedo (b), solar absorptivity (α), and emissivity (ϵ). Assuming that the terrain at the target site, Lacus Mortis, is covered with regolith, lunar albedo is determined using NASA's *Moon Fact Sheet* [12]. Using this value, lunar solar absorptivity is calculated, as shown in Equation 3. Note that this equation is valid if the surface is opaque.

$$\alpha + b = 1 \quad (3)$$

Lastly, emissivity is the ability of lunar surface to emit its heat via infrared energy. Since the emissivity differs by the wavelength as emitted by spectral radiation, we chose a value of 0.9 as a good approximation due to the small particle size of the lunar regolith mock up [13].
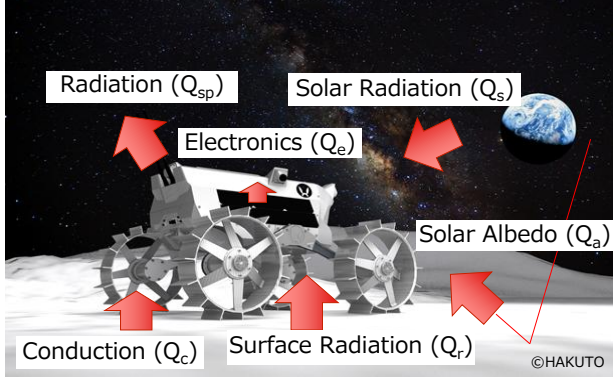
Figure 3. : *Thermal model and its corresponding heat input of the lunar rover*

3 THERMAL MODELING

A general thermal model of lunar rover is described in this section. This model is formulated based on the governing equations from energy and heat transfer. Overall thermal inputs to the rover are shown in Figure 3, where each thermal energy source is described in the following subsections.

3.1 Solar Radiation (Q_s)

In the lunar environment, solar radiation is one of the external heat sources that dominate the rover's temperature response. The heat equation is represented as follows:

$$Q_s = \alpha F A P_s \qquad (4)$$

where α is the solar absorptivity of the rover, F is the view factor between the solar flux and rover's planar surface, A is the cross sectional area of the rover, and P_s is the effective solar flux from the Sun to the Moon. Among these variables, α, A, and P_s are fixed once the rover's geometry and material is selected. On the other hand, the view factor between the solar flux and the rover's planar surface changes over time and based on latitude. The calculation process is shown in Section 3.1.1.

3.1.1 Effective view factor between rover surface and sun vector

The view factor calculation between the rover's surface and the sun is treated as a vector perpendicular to its planar surface. Figure 4 shows the rover and the sun vector, defined as $\vec{R_1}$ and $\vec{R_2}$ respectively. θ is the azimuth angle, ϕ is the zenith angle of the sun, and x is the rover's heading direction with respect to the sun. A spherical coordinate system is used to calculate the associated value in x, y, and z direction.

The effective solar vector angle (γ) in reference to the rover's planar surface is calculated by the dot product operator of $\vec{R_1}$ and $\vec{R_2}$ vectors, as shown in Equation 5. Alternatively, the orthogonality properties simplify the dot product operator into the Kronecker delta (δ_{ij}).

$$cos\gamma = \frac{\vec{R_1} \cdot \vec{R_2}}{\|\vec{R_1}\| \|\vec{R_2}\|} = \frac{\vec{R_1} \vec{R_2}^T \delta_{ij}}{\|\vec{R_1}\| \|\vec{R_2}\|} \qquad (5)$$

Using Equation 5, γ is calculated by taking the inverse cos of the dot product operation. Finally, in some rover orientations, the sun vector does not face the rover's surface (i.e. γ is determined as a negative value). To account for this condition, Equation 6 is used. The sin of this value represents an effective view factor from the sun to the rover's respective planar surface.

$$\gamma = \begin{cases} \gamma, & \text{if } \gamma \geq 0 \\ 0, & \text{if } \gamma < 0 \end{cases} \qquad (6)$$

3.2 Surface albedo (Q_a)

Thermal flux due to albedo (b) of solar radiation is determined by multiplying the albedo factor to Equation 4. The resulting equation is shown as follows:

$$Q_a = \alpha b F A P_s \qquad (7)$$

3.3 Infrared radiation (Q_r)

The heat exchange between two radiating surfaces is represented by the simple equation,

$$Q_r = \epsilon_i \epsilon_j F_{ij} A \sigma T_i^4 \qquad (8)$$

where ϵ_i is the emissivity of the emitting surface, ϵ_j is the emissivity of the intercepted surface, F_{ij} is the view factor from the emitting surface to the intercepted surface, and T_i is the temperature of the emitting surface. This equation enables calculation of any radiative heat exchange such as the lunar surface to the rover's surface (using the temperature model from Section 2.1) and between two associated bodies inside and outside the rover. The view factor from the lunar surface to the rover is calculated using a general analytical approach [14] or numerical analysis technique such as Monte Carlo Ray Tracing by software simulation.

3.4 Thermal conductivity (Q_c)

Among the different types of heat transfer process, thermal conduction has the highest influence on the rover. For the one-dimensional steady-state conduction through in the plane wall, the resulting heat equation is shown:
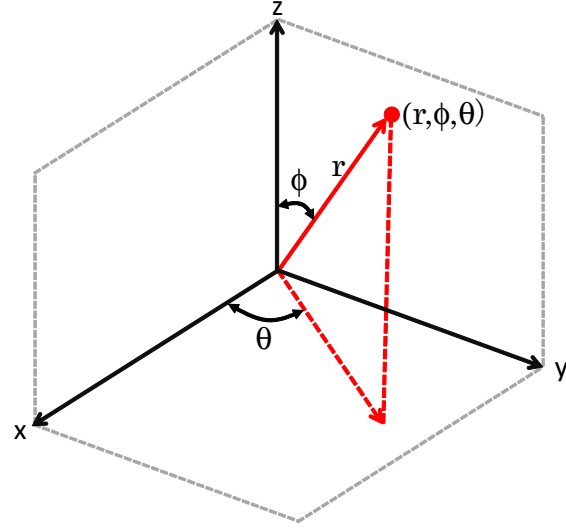
$$\frac{d}{dx} \left(\lambda \frac{dT}{dx} \right) = 0 \qquad (9)$$

where λ is the thermal conductivity and T is the temperature through the plane wall as a function of distance (x). Using boundary conditions of $x = 0$ and $x = L$, the resulting heat transfer rate is shown as the following,

$$Q_c = \lambda \frac{A}{L} (T_1 - T_2) \qquad (10)$$
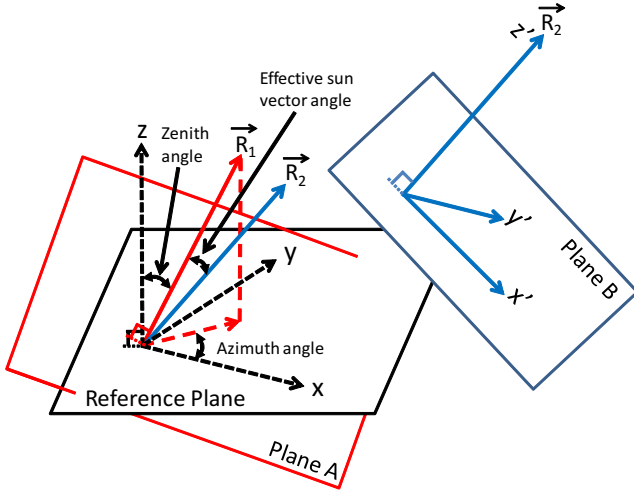
(a) Rover's surface vector (Plane A) and sun vector (Plane B)   (b) Spherical coordinate: azimuth (θ) and zenith angle (ϕ)

Figure 4. *: Vector transformation definition for the rover's planar surface area and the sun's planar vector*

where A is the cross sectional area of interest, L is the depth of the cross sectional area, and T_1 and T_2 are the temperatures at $x = 0$ and $x = L$ respectively. This equation assumes that every cross sectional area has a constant temperature. This assumption eases the heat rate calculation between the lunar surface and the wheel as well as between two mating surfaces associated with the rover. For a detailed analysis, a mesh calculation is used as described in Section 5.

For other one-dimensional steady state conduction such as for the cylindrical wall, the resulting heat equation (Equation 11) and heat flux (Equation 12) in a radial direction of cylindrical wall are as follows:

$$\frac{1}{r}\frac{d}{dr}\left(r\frac{dT}{dr}\right) = 0 \tag{11}$$

$$Q_C = \frac{\lambda(T_1 - T_2)}{r\ln(r_2/r_1)} \tag{12}$$

where r_1 is the inner radius and r_2 is the outer radius of the cylindrical wall. This equation is used for the wheel, motor, and motor housing as its geometric shape resembles closely to a cylinder.

3.5 Internal power source (Q_e)

All of the rover's internal power source is generated by the on-board avionics including the motor. To keep the battery size as small as possible, we chose all of the electronics with careful consideration to total of 20.1 W of power consumption for the actual mission. A detailed description on power distribution is given in Section 4.

3.6 Radiation to outer space (Q_{sp})

Thermal radiation from the rover to outer space is shown as:

$$Q_{sp} = \epsilon A\sigma(T_r^4 - T_{sp}^4) \tag{13}$$

where T_r is the rover's surface temperature, σ is the Stefan-Boltzmann constant, ϵ is the emissivity of the rover, and T_{sp} is the temperature of outer space. Using the definition from cosmic microwave background, the T_{sp} of 2.73 K is applied.

3.7 Equilibrium model

By combining the above thermal inputs, we can describe the overall thermal model at equilibrium state using the simple expression as follows:

$$Q_s + Q_a + Q_r + Q_c + Q_e = Q_{sp} \tag{14}$$

This back-of-the-envelope equation enables a quick rover temperature calculation, thereby allowing several trend studies and reiterations by changing the rover's thermal parameters.

3.8 Numerical calculations

Until now, the thermal model is calculated under the assumption that each heat input and output are independently calculated at a specific nodal surface point. Furthermore, the thermal inputs are not processed in a time varying function due to computational difficulties in calculating both radiation and conduction simultaneously. For this reason, numerical software such as MATLAB, Solidworks, NASTRAN, and Thermal Desktop are used to compute the thermal model using a fine mesh with nodal points (i and j). The general 1st order differential equation is expressed as following:

$$m_i c_{pi} \frac{dT_i}{dt} = Q_i - \sum_{j=1}^{n} C_{ij}(T_i - T_j) -$$
$$\sum_{j=1}^{n} \epsilon_i \epsilon_j F_{ij} A_i \sigma (T_i^4 - T_j^4) \qquad (15)$$

where m_i is the mass, c_{pi} is the specific heat, Q_i is the thermal input and output to the rover, C_{ij} is the heat transfer coefficient, ϵ_i and ϵ_j are the emissivity, T_i and T_j are the temperature at the specific nodal point, F_{ij} is the view factor, A_i the cross sectional area, and σ is the Stefan-Boltzmann constant.

4 FM ROVER'S DESCRIPTION

The FM rover consists of several subcategories: the body, thermal isolator, avionics, the motors, and the wheels. The main structural support of the rover is fabricated out of carbon fiber reinforced polymer (CFRP), which is intended to reduce the weight of the rover as much as possible. Alternatively, aluminum is used for locomotive components to increase their rigidity. From a thermal aspect, CFRP itself is not a conductive material for effectively transferring avionics heat to outer space. For that purpose, we mount Magnesium (Mg) alloy between the CFRP structure. All of the avionics are attached to a Mg alloy radiative surface as shown in Figure 5. With a triple-junction GeInP/GaAS/Ge solar panel attached on the side surface, all of the avionics are attached to the front, top, and rear surfaces of the rover. The avionics are not attached to the bottom surface due to high lunar surface temperature at mid-day, which exceeds the operational temperature range for several avionics components.

During operation, solar cells are expected to absorb solar energy, which consequently increases its temperature. To minimize the heat transfer from the solar panel to the cool radiative surface, we inserted a low conductive printed polyetherimide material, ULTEM, between the two surfaces to act as a thermal isolator. Likewise, the same thermal isolation principle is used for the wheel's material and between the bottom and upper surface to decrease the effect of lunar surface heat flux. Furthermore, the rover's inner surface is plated with material with low emissivity (i.e. silver sheet) to minimize the radiative heat transfer between the two surfaces. In terms of mobility, each motor independently controls a wheel for maneuvering while using skid steering for a spot turn. To reduce the amount of regolith contact, the motor is covered with an Aluminum (Al) housing. Additionally, Silver (Ag) Teflon is coated onto the rover's emissive surface (i.e. body, motor housing, and wheel) to decrease the solar flux input and to increase its emissivity to outer space.

The rover's geometric shape is decided based on both the allowable design constraints and the optimal thermal
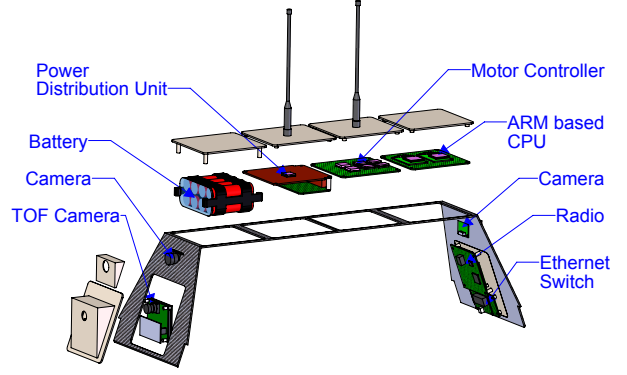

Figure 5. *: Interior hardware placement*

Table 1. *: Weight and power distribution of FM rover*

Component	Mass (g)	Power (W)
4 Wheels	800	0
Mechanical Parts	800	0
CFRP Body	472	0
4 Brushless Motors	524	12
Motor Controller	40	1
Power Unit	105	0.5
IMU	10	0.1
Ethernet Switch	35	1
80Wh Battery	473	1
Solar Cells	320	0
Wiring	80	0.3
4 Lens	50	0
Two 5MP Camera	25	0.5
Two 1.3MP Camera	25	0.35
Time of Flight (TOF) Camera	100	1
Two Main Controllers	90	1.4
Radio	76	0.75
Mass memory (emmc)	0	0
Interface boards (I/F)	100	0.2
Totals	4125 g	20.1 W

performance of the rover. We determined front and rear angles between 60° and 75° to fit the lander's size constraint while decreasing lunar surface heat radiation by view factor relationship. On the other hand, a side surface angle of 70° is chosen based on the target landing site, thermal performance, and optimal power generation to sustain power consumption above the minimum required throughout the entire mission [5].

Table 1 shows the FM rover's gross weight and power consumption. Each of the components is carefully selected based on space legacy and COTS availability. The gross weight of the rover is about 4 kg while maintaining the power consumption as low as possible. A detailed description of the system architecture is described in the next section.
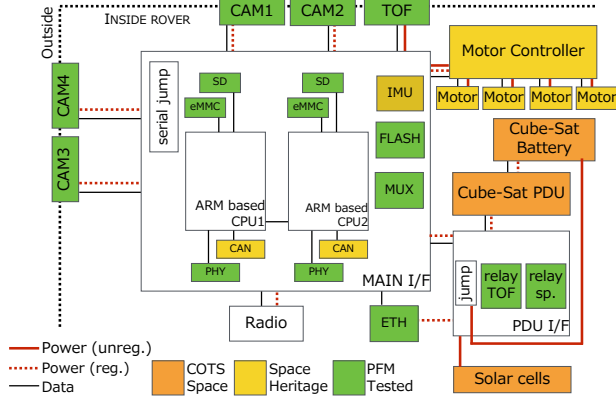
Figure 6. *: Moonraker FM internal hardware system architecture*

4.1 Hardware system architecture

The current system architecture of the FM rover is shown in Figure 6. Several space ready COTS components and heritage electronics from RISING-2 and PFM rovers are carried over to prepare the FM rover for the launch while improving the thermal performance. This is reflected in the change of the main controller (ARM based CPU) and the 3D sensor (Time of Flight Camera, TOF), where the mass and power consumption is reduced by more than half while retaining the same or better performance from that of the PFM rover. Furthermore, the usage of two main controllers instead of one controller increases redundancy. This is possible due to better power management. For imaging components, we select four different camera set-ups (two of them are the fish eye cameras, and the other two are 135° fields of view cameras) instead of the omni-directional camera. This increases both the overall imaging qualities and the robustness from potential multiple failure mode during the mission. On the other hand, all newly introduced hardware requires extensive testing for space qualification, which is vital to assess its functionality in a space environment.

4.2 Material selection

Material selection for the FM rover is shown in Table 2, where detailed thermal properties are described. Most of these parameters are published data from online sources. However, these parameters require verification through thermal vacuum testing to increase their reliability when every component is integrated together.

4.3 Hardware temperature limit

Table 3 shows the on board avionics' operational temperature ranges for the FM rover. We selected hardware that is designed for automotive purposes (i.e. main controller), thereby increasing the operable temperature range compared to a previous controller. This allows flexible attachment within the limited space inside the rover while re-

Table 2. *: Moonraker FM material*

Material	λ	c_p	ϵ	α
CFRP	10	795	0.80	0.80
Stainless steel	17	510	0.56	0.80
Al 7075-T6	130	960	0.06	0.25
ULTEM	0.1225	1470	0.84	0.40
Magnesium alloy	156	1050	0.07	0.39
Ag Teflon	5.02	1400	0.76	0.17
Solar panel	66	320	0.85	0.92
λ-gel	2.60	1150	0.79	N/A
FR4	0.22	1386	0.75	N/A

Table 3. *: Moonraker FM hardware operational temperature range*

Hardware	Temperature (deg C)	
	Minimum	Maximum
Motor	-40	100
Camera	-40	85
Time of Flight Camera	-40	85
Ethernet Switch	-40	60
Motor Controller	-20	70
Power Distribution Unit	-40	85
Radio	-40	85
Battery in Discharge	-20	60
Battery in Charge	-5	45
IMU	-40	100
Arm based CPU	-20	125

Table 4. *: Temperature range chart for avionics at corresponding surface*

Description		Requirement
Front Surface	GLXP Mission	-40 ~ 85°C
	Lunar Day Mission	-40 ~ 85°C
Top Surface	GLXP Mission	-20 ~ 45°C
	Lunar Day Mission	-20 ~ 45°C
Rear Surface	GLXP Mission	-40 ~ 85°C
	Lunar Day Mission	-40 ~ 85°C
Power Generation	GLXP Mission	≥20.1 W
	Lunar Day Mission	≥20.1 W

ducing thermal build-up risk within each other.

From Figure 5, each component is mounted at specific locations to prevent thermal saturation. Using Table 3, the absolute operational temperature range for each radiating surface is defined (Table 4). Note that there are no differences in the rover's operational requirement at two different missions (GLXP and lunar day). For power generation, we selected a power above 20.1 W as a minimal requirement based on the information provided in Table 1 to fully operate the rover at 100% of its required specifications.
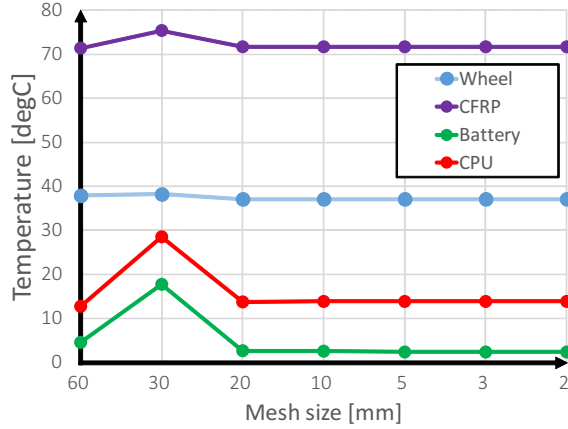
Figure 7. *: Mesh convergence size*

5   RESULT

The rover's thermal performance was calculated using the Solidworks simulation analysis tool. Thermal parameters were chosen based on Section 4.

5.1   Simulation parameters

We apply two types of mesh grid to compute the model. For components with low thermal load (i.e. body, leg, wheel, etc.), we select a curvature based mesh with a size between 6 mm and 20 mm. As these parts are not the region of main interest, a relatively large mesh width enables the reduction of the required amount of computation time. On the other hand, we chose a mesh size of 2 mm with an aspect ratio of 1.5 for the heat generating element (i.e. the on-board electronics). As the IC chip's dimension is on the order of 10 mm, a mesh with more nodal elements is required to increase the computational precision of the model. Figure 7 shows the mesh size convergence for the temperature critical electronics (battery and PDU) and non-temperature bounded components (CFRP and wheel), verifying that the former and the latter require a minimum of 20 mm and 5 mm for computation precision.

To simulate the worst case condition, the solar vector is set to face toward the rover's side surface. This orientation expects a heat build-up on the solar panel, where its energy is subsequently transferred as thermal conduction to the avionics mounted surface.

The heat source by electronics is defined as following. All of the avionics expect for the motor use the same power consumption values from Table 1 as the heat emission measured in watts. For the motor, 67% of its power consumption is translated into heat, whereas the rest of the power is converted into kinetic energy during mobility.

5.2   Simulation

Figure 8 shows the temperature profile of the FM rover. This simulation calculates the FM rover's equilibrium
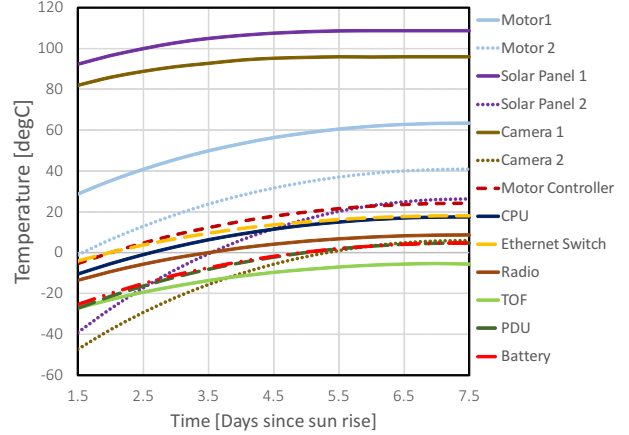

Figure 8. *: Temperature profile of the FM rover at equilibrium state. Components that are directly influenced by solar radiation (motor, solar panel, and camera) are annotated with 1 at the end and vice versa with 2 at the end.*
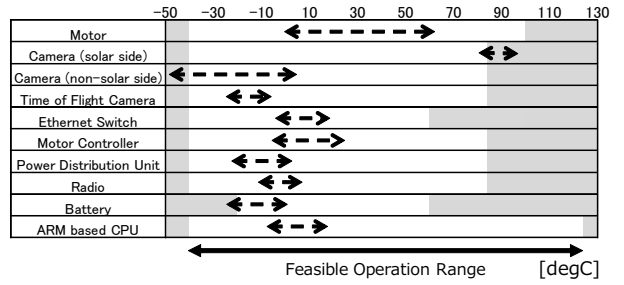

Figure 9. *: Simulated operational temperature profile of the FM rover*

state every 12 hours from the mission start (1.5 days after sunrise) to beyond lunar mid-day (7.5 days after sunrise). As expected, the solar panel facing the sun has the highest temperature. Other than the camera facing the sun (Camera 1), all of the avionics are capable of operating throughout the lunar day without the risk of overheating. Although several components are slightly below the operational temperature range at the start of mission, we expect these components to increase their temperature over time. The resulting operational temperature summary is shown in Figure 9, where the dotted black line indicates the simulation result for each on-board electronics. The white region represents the feasible operational temperature range for each avionics, terminating from gray colored zone.

There are several potential solutions to improve Camera 1's thermal performance. First, we determined the need for non-conductive material installed between the side surface and the camera to reduce the thermal conduction effect from the solar panel. Another option is to thermally control the rover's heading orientation over time. From Figure 8, camera facing away from the sun is within the operational temperature. This suggests that a zigzag

like locomotive path along the terrain is favorable to release the heat in a timely fashion. Similarly, a parking limitation is seen with the Lunar Roving Vehicle to prevent overheating during the mission [15]. Therefore, thermal management is required to protect the camera from reaching beyond operational temperature limit.

6 CONCLUSION

This paper has presented the thermal design step for the ongoing lunar micro rover. We utilize computational tool to simulate the thermal response of the new Moonraker FM design in the expected lunar environment conditions. Based on the worst case scenario, we determined that onboard avionics, except for the camera facing the sun, are within temperature tolerance levels. Thus, verifying the feasibility of the new thermal design strategy. To update the parameter tuning for the simulation, we anticipate to conduct thermal vacuum testing using actual flight model components. This research culminates in the system design requirements for the HAKUTO lunar microrover Flight Model thermal interface with construction, integrated thermal vacuum testing, and lunar surface operations are considered as a future work.

Acknowledgment

References

[1] Britton N, et. al. (2013) Lunar Micro Rover Design for Exploration through Virtual Reality Teleoperation. *In: proceedings of 9th Field and Service Robotics*, Brisbane, Australia.

[2] Walker J, Britton N, Yoshida K (2015) Operation of a Lunar Rover with a Redundant Microcontroller and Multiple Camera Architecture. In: *proceedings of 25th Workshop of JAXA Astrodynamics and Flight Mechanics*, Kamakura, Japan.

[3] Walker J, et. al. (2015) Update on the Qualification of the Hakuto Micro-Rover for the Google Lunar X-Prize. In: *proceedings of 10th Field and Service Robotics*, Toronto, Canada.

[4] Oikawa T, Walker J, Yoshida K (2015) Experimental Evaluation of Thermal Simulation Model for Lunar Exploration Rover. In: *proceedings of 2015 IEEE/SICE International Symposium on System Integration (SII)*, Nagoya, Japan, pp.882-887.

[5] Oikawa T (2016) *Thermal Design and Analysis of Lunar Micro Rover*. Master's Thesis, Tohoku University, Sendai, Japan.

[6] Hammond W (2001) *Design Methodologies for Space Transportation Systems*. AIAA Education Series

[7] Sakamoto Y, et al. (2010). Pre-Flight Analysis, Test Evaluation and Flight Verification of the Thermal System of Tohoku University SPRITE-SAT. In: *Transactions of Japan Society for Aeronautical and Space Sciences*, vol. 8, pp. 1-6

[8] Baturkin V (2005) Micro-satellites thermal control concepts and components. *Acta Astronautica*, vol. 56, pp. 161170

[9] Hurley D, et al. (2014) An analytic function of lunar surface temperature for exospheric modeling. *Icarus*, vol. 255, pp. 159-163

[10] Vasvada A R, et al. (2012) Lunar equatorial surface temperature and regolith properties from the Diviner Lunar Radiometer Experiment. *Journal of Geophysical Research Atmospheres*, vol. 117, E00H18

[11] Walker J (2016) *Scalable Flight System Design of Lunar Microrovers*. Doctoral Thesis, Tohoku University, Sendai, Japan.

[12] William D R (2016) *Moon Fact Sheet*. url: http://nssdc.gsfc.nasa.gov/planetary/factsheet/moonfact.html

[13] Gaier J R, et al. (2010) *Measurement of the Solar Absorptance and Thermal Emittance of Lunar Simulants*. Technical Memorandum NASA/TM2010-216788, Glenn Research Center, Cleveland, Ohio, USA

[14] Martinez (2016) *Radiative View Factor*. url: http://webserver.dmt.upm.es/~isidoro/tc3/Radiation%20View%20factors.pdf

[15] Boeing Company (1971) *Lunar Roving Vehicle Operations Handbook (contract NASB-25145)*. Huntsville, Alabama, USA.